nature communications

Article

https://doi.org/10.1038/s41467-025-59023-7

Electrically-driven phase transition actuators to power soft robot designs

Received: 17 October 2024

Accepted: 3 April 2025

Published online: 25 April 2025

Check for updates

D. Fonseca & P. Neto

In the quest for electrically-driven soft actuators, the focus has shifted away from liquid-gas phase transition, commonly associated with reduced strain rates and actuation delays, in favour of electrostatic and other electrothermal actuation methods. This prevented the technology from capitalizing on its unique characteristics, particularly: low voltage operation, controllability, scalability, and ease of integration into robots. Here, we introduce a liquid-gas phase transition electric soft actuator that uses water as the working fluid and is powered by a coil-type flexible heating element. It achieves strain rates of over 16%/s and pressurization rates of 100 kPa/s. Blocked forces exceeding 50 N were achieved while operating at voltages up to 24 V. We propose a method for selecting working fluids which allows for application-specific optimization, together with a nonlinear control approach that reduces both parasitic vibrations and control lag. We demonstrate the integration of this technology in soft robotic systems, including a cable-driven biomimetic hand and a quadruped robot powered by liquid-gas phase transition.

Nature is a rich source of inspiration for soft roboticists[1,2], who often learn from observing various forms of animal and plant life thereby creating innovative robot designs[3–7]. This bioinspired approach steers research towards tackling complex challenges such as locomotion and manipulation in unstructured environments. Soft robots are becoming ever more complex systems, dependent on multiple core technologies, including: materials, fabrication processes[8–10], sensors[11,12], electric conductors[13,14], and actuators[1,15]. Various energy sources have been used to power soft actuators, namely: pressurized fluids[16–19], chemical energy[6,20–22], heat[7,23–25], magnetic or electric fields[26–29] and electric current[30,31].

Electrically-driven soft actuators are of particular importance due to the practicalities of storing, transmitting, and controlling electric energy. The use of electronic circuits to control soft robots enables logic and communication capabilities beyond those of on-board microfluidic logic systems[32–35]. Electric soft actuation has been achieved through various methods. Electrostatic actuators, such as Dielectric Elastomer Actuators (DEAs) and Hydraulically Amplified Self-Healing Electrostatic Actuators (HASELs)[36–38], utilize Maxwell stresses to deform their structure. Piezoelectric actuators rely on the reverse piezoelectric effect to generate work[39,40]. Electrochemical actuators rely on pressure gradients resultant from electrolysis[41], intercalation processes[42–44] or redox reactions[45–47]. Electrothermal actuators use heat as an intermediary form of energy that is then converted into work through thermal expansion or phase transitions. Given the unique features and characteristics of each actuation technology, we believe it is key to develop them all to a stage at which their full potential can be thoroughly evaluated.

Let us consider electrothermal actuators. Compared to their electrostatic counterparts, they tend to operate at lower voltages (Fig. 1a), and are usually resistive electric loads[48]. This combination not only reduces the risk of electromagnetic interference but also allows for safer and simpler driver circuits. Electrothermal actuators can also achieve some of the highest work densities[1,16], making them particularly attractive for applications requiring actuation in compact designs. However, these benefits come with well-known trade-offs. Electrothermal actuation typically suffers from low strain rates (Fig. 1b), preventing them from being deployed in high-speed applications. Furthermore, technologies based on fiber-like thin structures, common in Shape Memory Alloys (SMAs), Twisted-and-Coiled Actuators (TCAs)[49], and Liquid Crystal Elastomers (LCEs)[50], can be troublesome to scale up due to limitations regarding physical integrity and thermal stress. Safety concerns arising from high operating temperatures must also be considered when implementing electrothermal soft actuators.

University of Coimbra, CEMMPRE, Department of Mechanical Engineering, Coimbra, Portugal. e-mail: pedro.neto@dem.uc.pt

https://doi.org/10.1038/s41467-025-59023-7

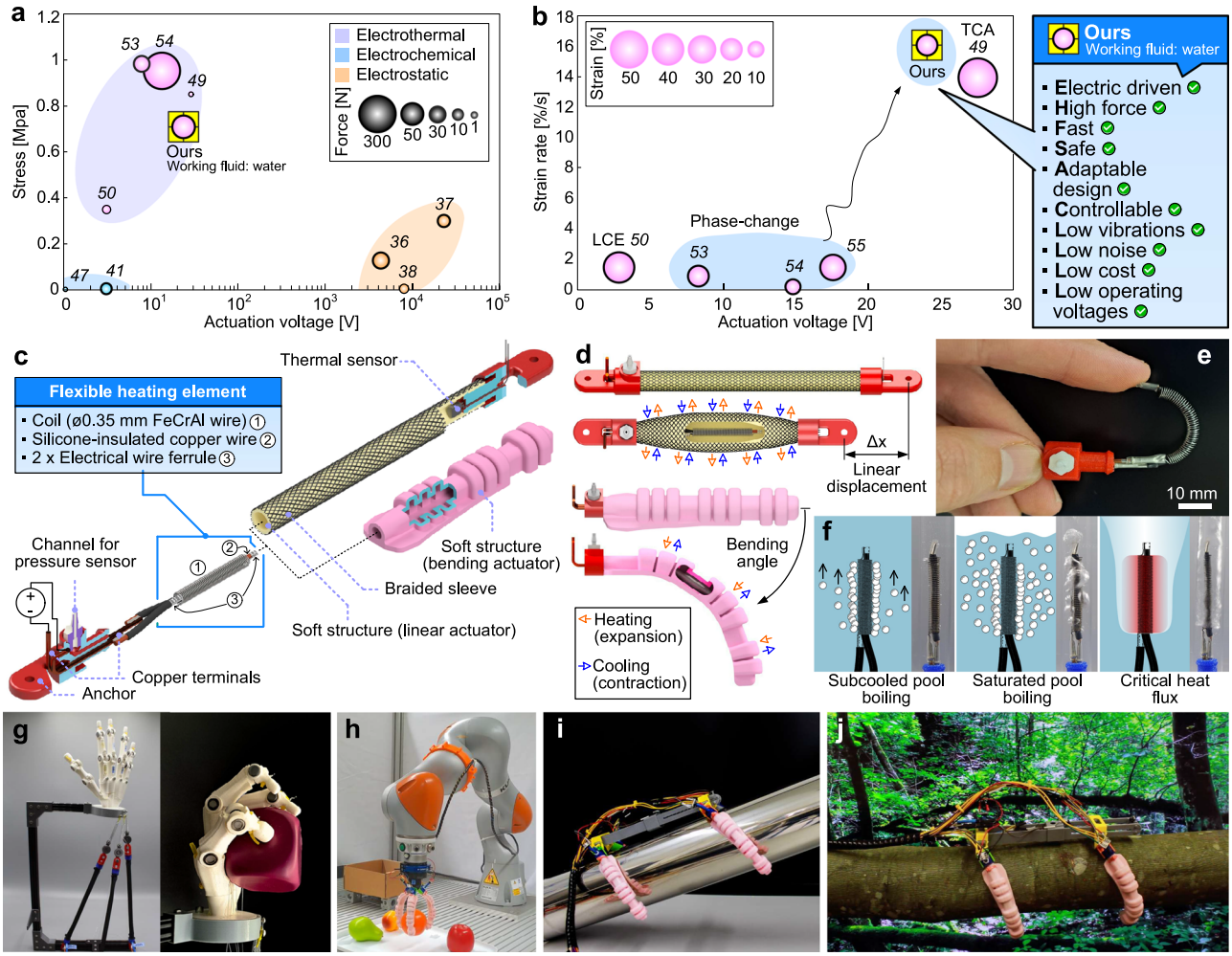

Fig. 1 | Liquid-gas phase transition actuator: comparative performance, design, working principle and robot prototypes. a Literature survey of electric linear soft actuators (stress and force with respect to actuation voltage). **b** Literature survey of electrothermal linear contractile actuator performance (strain and strain rate with respect to actuation voltage). **c** Design and exploded view of the linear and bending actuators. **d** Actuation principle based on pressure generated through liquid-gas phase transition. **e** Actuator core with flexible heating element. **f** Operating regimes: subcooled pool boiling, saturated pool boiling and critical heat flux. **g** Biomimetic hand powered by linear phase transition soft actuators. **h** Soft robotic gripper powered by bending phase transition soft actuators. **i** Bixo robot powered by four phase transition actuators, crawling on an inclined metallic tube. **j** Bixo robot crawling on a horizontal tree trunk.

In this work, we focus on the particular case of liquid-gas phase transition actuators, where a liquid working fluid is heated and vaporized, creating pressure that deforms soft structures[51]. Since the working fluid provides uniform pressure distribution, liquid-gas actuators are potentially less susceptible to thermal stress and offer higher design flexibility when compared to other phase transition actuators such as LCEs, where actuation is dependent on the alignment of liquid crystal molecules[52]. This design flexibility is demonstrated in Fig. 1c, d, where actuators with different actuation modes can share the same internal components. The decoupling between pressure-generating components, heating element and working fluid, and external soft structures also allows actuators to be optimized to achieve highly specific actuation modes. This design ensures they are robust enough to operate in direct exposure to the outside environment, eliminating the need for additional protection provided by the robot's main structure.

However, liquid-gas phase transition actuators exhibit significant limitations. They feature low strain rates, often with multi-second delays, even when compared to other electrothermal technologies (Fig. 1b). Contractile strain rates sit currently in the range of 1–2%/s[53–55]. They also face rapid degradation of performance due to the depletion of the working fluid by diffusion through the actuator's structure[56,57]. Surprisingly, our experimental findings also revealed that these actuators are subject to mechanical vibrations, an issue that has been seemingly overlooked in previous literature. We demonstrate that these instabilities stem from operating in thermodynamically unsaturated boiling regimes[58,59] and can be significantly mitigated through the implementation of appropriate control strategies. We also demonstrate how these same control strategies can effectively reduce actuation delays.

Apart from addressing existing limitations, we set out to explore the untapped potential of liquid-gas phase transition. We start by introducing an innovative actuator design (Fig. 1d, e), and propose a systematic approach to selecting the working fluid that enables application-specific temperature and pressure optimization. The selection of working fluids opens an opportunity to fine-tune operating temperatures to meet specific application requirements. Although no comprehensive methods for working fluid selection have been previously proposed in the context of soft actuators, foundational experimental research has already been outlined[60].

To further enhance performance, a nonlinear control strategy is proposed, capable of effectively mitigating parasitic vibrations and reducing control lag. We then investigate pressurization limitations, including the limit imposed by Critical Heat Flux (CHF), Fig. 1f, demonstrating a pressurization rate of 100 kPa/s. These performance

figures suggest the feasibility of a class of high-performance liquid-gas phase transition actuators.

Finally, we demonstrate how the proposed actuator design can be integrated into compliant mechanical systems by developing a cable-driven biomimetic hand, a soft robotic gripper, and Bixo, a quadruped robot powered by liquid-gas phase transition actuators, Fig. 1g–j. The aim of this work is to provide a good understanding of the untapped potential and limitations of this underexplored actuation technology, which we believe will play a significant role in the development of future untethered soft robots[16].

Results

Design guidelines

To unlock a class of high-performance liquid-gas phase transition actuators, a critical review of previous design concepts is required. While maintaining the underlying principle of creating pressure inside a soft structure by boiling a working fluid, different methods have been proposed, posing multiple questions whose answers shape the design. Working fluids can be held in bulk inside a pressure chamber[55] or suspended in a silicone matrix[56]. Heating elements may or may not be designed to have direct contact with the working fluid[7,27]. The electric energy required to power the heating element may be wired through internal conductors or transmitted wirelessly[53]. Useful work can be generated using various soft structures, including McKibbens, bellows, pneu-nets and pouches.

Our design concept (Fig. 1c) reflects a prioritization of high heat flux capacity and design modularity. The working fluid is stored in bulk to avoid the thermal mass of an inert matrix. The heating element is in direct contact with the fluid to reduce the thermal resistance between the two. Additionally, electric power is directly wired to the heating element using internal conductors, which simplifies the overall actuation system and avoids the losses associated with wireless power transmission. In the proposed linear actuator variant, we included the option for two redundant state variable sensors, both an internal temperature and an internal pressure sensor. However, as will be shown and discussed shortly, we later concluded that pressure-based control is preferable, so we refrained from including temperature sensors in the bending actuators, which allowed for an even simpler design. A pressure tap, used to connect the pressure sensor, also allows for the working fluid to be replaced or replenished, if necessary, effectively removing the main life-limiting factor of previous designs.

Some of the previous design decisions raise concerns regarding reliability. The use of a working fluid in bulk implies that actuators will fail in the event of a single leak, while direct contact between the heating element and the fluid increases the risk of oxidation or chemical incompatibility. The routing of electric conductors into the pressurized soft structure also introduces pathways and joint interfaces that are prone to leaks. These concerns were addressed by following a modular design approach that enabled rapid iteration at the component level, as well as using monolithic elastomer structures for all the soft structures. The linear actuator variant is based on the well-established McKibben design, due to its simplicity and robustness, while the bending actuator variant is based on a fast Pneu-Net (fPN) design (Fig. 1c, d), which is one of the highest performing geometries for pneumatic soft bending actuators[61]. Details on the design and fabrication of all actuator components, including the heating element and soft structure, are available in Supplementary Notes 2 and 3.

Actuation principle

The boiling of a bulk mass of fluid confined within a hermetically sealed soft actuator can be approximated as a form of pool boiling. When the heating element's surface temperature rises above the local saturation temperature of the fluid, vapor bubbles nucleate and increase in size until buoyant forces cause them to detach. These gas bubbles are initially not in thermodynamic equilibrium with the adjacent liquid phase, which results in a transfer of heat between the two phases, liquid and gas. While the temperature of the liquid phase is kept lower than its saturation temperature, vapor bubbles tend to collapse before they reach the liquid's free surface, a regime known as subcooled pool boiling (Fig. 1f and Supplementary Movie 1). When the liquid temperature gets sufficiently close to saturation, vapor bubbles will rise all the way to the surface, entering a regime known as saturated pool boiling. The effect of bubble collapse under subcooled pool boiling is similar to the phenomena of cavitation, and results in pressure shock waves that compromise the integrity of the actuator. These bubble collapses are also the main source of instability causing mechanical vibrations in the soft actuator. To avoid premature failure and reduce the magnitude of actuator vibrations, we propose a control strategy which aims to maintain actuators in thermodynamic saturation during the entire actuation cycle. Vibrations, or any other form of actuation instability, significantly impact the implementation of actuators in delicate mechanical systems, including soft robots. Additionally, vibrations are a primary source of acoustic noise, which can be a critical factor for operations in noise sensitive environments.

An effective controller should also make full use of the actuator's heat flux capacity, providing as much peak power as the actuator can safely handle. The thermodynamic limit for this heat transfer rate is reached when an excess of vapor bubbles coalesce, creating a gaseous layer that separates the heating element's surface from the liquid phase. At this point, the thermal resistance increases significantly as heat is now being transferred through a solid-gas interface and, as a result, the surface temperature of the heating element will increase accordingly, compromising the integrity of the system. The heat flux at this point is known as the Critical Heat Flux (CHF) and sets a practical limit to the pressurization rate of liquid-gas phase transition soft actuators[62].

Working Fluid Selection

The selection of the working fluid is an important opportunity to fine-tune actuators to meet specific application requirements. We introduce a four-step selection method based on thermodynamic and safety data. Step one involves selecting fluids based on the desired actuator operating pressure and temperature ranges. We started by excluding fluids that are not liquid at ambient temperature and pressure (20°C, 101.33 kPa). We then selected an upper temperature limit of 138°C, which is the softening temperature of the actuator's polyurethane components. A maximum relative pressure limit of 130 kPa was also defined, based on a safety factor of 2 applied to early destructive test data. Fluids outside these ranges are excluded (Fig. 2a), specifically R-11 and toluene.

Step two involves an evaluation of fluid-material compatibility. Fluorine-based fluids, including the Novec series of engineering fluids (3 M, USA), as well as ethanol, are known to swell and diffuse through silicones and natural rubber[63–66]. Water has been demonstrated to have lower diffusion rates through silicone[64], suggesting a longer life expectancy for the actuators. Accordingly, in this step we excluded all fluorinated fluids and ethanol.

Step three assesses fluid safety, toxicity, and sustainability. Fluids with low flashpoints, such as acetone or ethanol pose fire hazards, and some have significant acute toxicity. Available information on toxicity parameters and symptoms of exposure is compiled in Supplementary Table 4 and 5. The simple, robust design of these actuators makes them suitable for unprotected use in various environments, making their sustainability heavily dependent on selecting fluids with minimal environmental impact. A compilation of the ecotoxicological data available is shown in Supplementary Table 6. This step identified water as the safer alternative.

Step four benchmarks' fluids using a custom metric we named the boundary work coefficient (ω_b). This coefficient is the ratio of work done by the expanding fluid to the heat provided, assuming an

https://doi.org/10.1038/s41467-025-59023-7

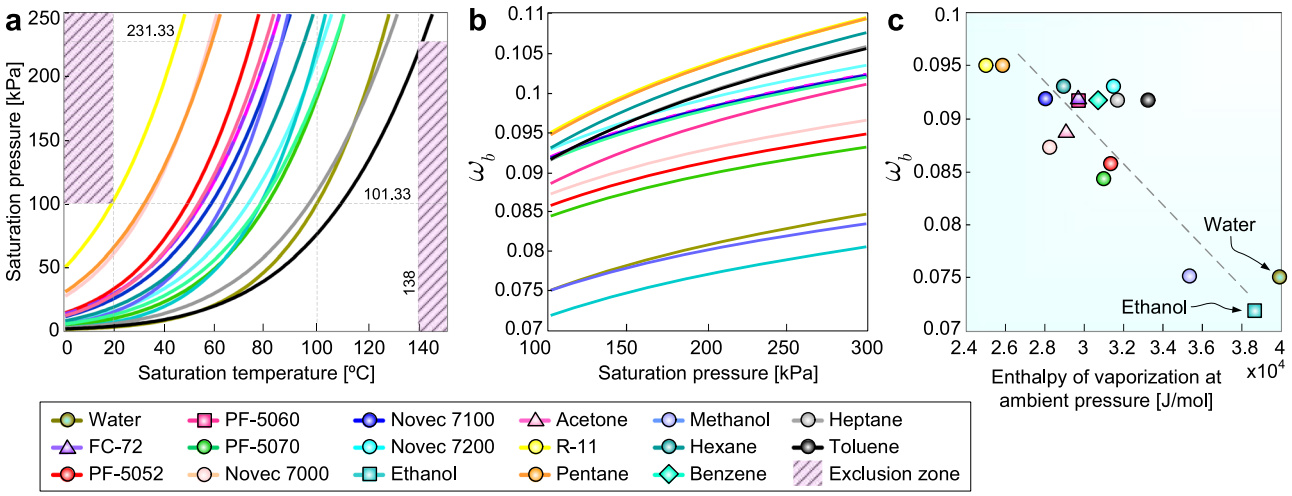

Fig. 2 | Fluid data for the five-step selection method. a Saturation pressure relative to the saturation temperatures. **b** Boundary work ratio relative to the saturation pressure. The boundary work ratio is the ratio of the boundary work done by the expanding fluid to the heat provided. **c** Boundary work ratio relative to the enthalpy of vaporization at ambient pressure. The dashed line illustrates the underlying trend observed across the different fluids.

idealized isobaric expansion. It can be calculated from the fluid's pressure-temperature saturation curve, critical temperature, enthalpy of vaporization, and molar weight. Results are shown in Fig. 2b, c. A comprehensive step-by-step example of the calculation procedure is detailed in the Supplementary Note 1. While ω_b does not represent actual actuation efficiency, it is useful for comparing fluids. Data suggest a negative correlation between enthalpy of vaporization and ω_b, so we recommend giving preference to fluids with lower enthalpy of vaporization. While recent experimental observations have shown no evident correlation between the enthalpy of vaporization and maximum actuation strain[60], selecting fluids with a higher enthalpy of vaporization could allow for higher CHF values[67] and, potentially, increase the maximum pressurization rate at which a given actuator design may operate. However, as we will demonstrate, the current limiting factor for actuation cycle speed is the rate of condensation during the cool-down period, which is not directly related to the CHF. Moreover, for our actuators, we prioritized safety, selecting low-toxicity, non-flammable fluids without hazardous byproducts, low mass diffusivity through silicone, and ample thermodynamic data availability, leading us to choose water. The higher enthalpy of vaporization of water suggests our performance figures are conservative baselines for future high-performance actuators.

Influence of elastomer hardness

The level of decoupling between the different actuator components, characteristic of our modular design, creates an opportunity to develop actuator soft structures with a greater focus on the application requirements, while being subjected to fewer constraints internal to the actuator. In particular, the separation between the work generating component (working fluid) and the soft structure itself, allows us to approach the selection of elastomer materials with a focus on increasing performance figures such as strain rates, actuation force, or stability under external loads.

To verify the influence of the elastomer material on actuation performance we fabricated four geometrically identical linear actuators, each of them using a different elastomer for their soft structure. The chosen elastomers consisted of a variety of platinum-cured silicones (Ecoflex 00–30, Ecoflex 00–50, and Smooth-Sil 940 from Smooth-On, USA) alongside natural rubber. This material selection spans a range of hardness levels extending from Shore 00–30 to Shore 00–80. The actuators were then subjected to isometric and isotonic testing to evaluate differences in performance. For the isometric testing setup, each actuator was driven by a Proportional Integral (PI) controller which was commanded to pressurize it at a rate of 1 kPa/s (Fig. 3a). A linear pressure-force response was observed across all the actuators, with force slopes monotonically increasing with decreasing material hardness (Fig. 3b). This effect can be leveraged to adjust the actuator's operating pressures according to the application requirements without the need for geometric design adjustments. It also highlights the importance of selecting elastomer material in conjunction with the working fluid to ensure that both the operating pressures and temperatures meet the application requirements. The maximum blocked force achieved during the test was 52 N, achieved by the Ecoflex 00–30 actuator at 308 kPa (Fig. 3b).

We then evaluated isotonic performance by performing five cycles of pressurization/depressurization, also at a rate of 1 kPa/s while acting against a constant load of 10 N (Fig. 3c). Comparing the force gains allowed by softer materials, observable in Fig. 3b, to the displacement gains allowed by the same materials in Fig. 3c leads us to conclude that the use of softer elastomers increases displacement more than they increase force. As a result, we selected the softest material (Ecoflex 00–30) to fabricate all subsequent linear actuators. Additionally, no significant hysteresis was observed in the isotonic test, consistent with the behavior of traditional pneumatic McKibben actuators[68,69]. Under no load conditions, a linear actuator made of Ecoflex 00–30 achieved a contractile strain rate of 16.6%/s. The actuator proceeded to reach a maximum unloaded contractile strain of 27%, which is consistent with the performance of pneumatic McKibben soft actuators[70].

We then used the actuator made of Ecoflex 00–30 to obtain more comprehensive isotonic data by subjecting it to various loads while measuring their maximum displacement (Fig. 3d). Tests at higher loads were extended to 200 kPa, allowing us to achieve a realistic assessment of the actual work output capability, unconstrained by our empirically defined safety limit of 130 kPa. During these tests, the maximum work output was 0.56 J, corresponding to a specific energy of ~30 J/kg and an energy efficiency of 0.11%. Regardless of power settings, the actuator reached peak efficiency when actuating against an 18 N load, as detailed in Supplementary Note 7. Finally, the selection of the material for the soft structure of the bending actuator needed to ensure sufficient stiffness to avoid unwanted bending under the influence of gravity. We settled for Smooth-Sil 940 due to its higher hardness value (Shore 00–80). A flat membrane was also included in the design to increase structural stiffness under lateral loads. The bending coefficient, a metric proposed to compare different bending actuator designs, and which consists of the ratio of curvature over input

https://doi.org/10.1038/s41467-025-59023-7

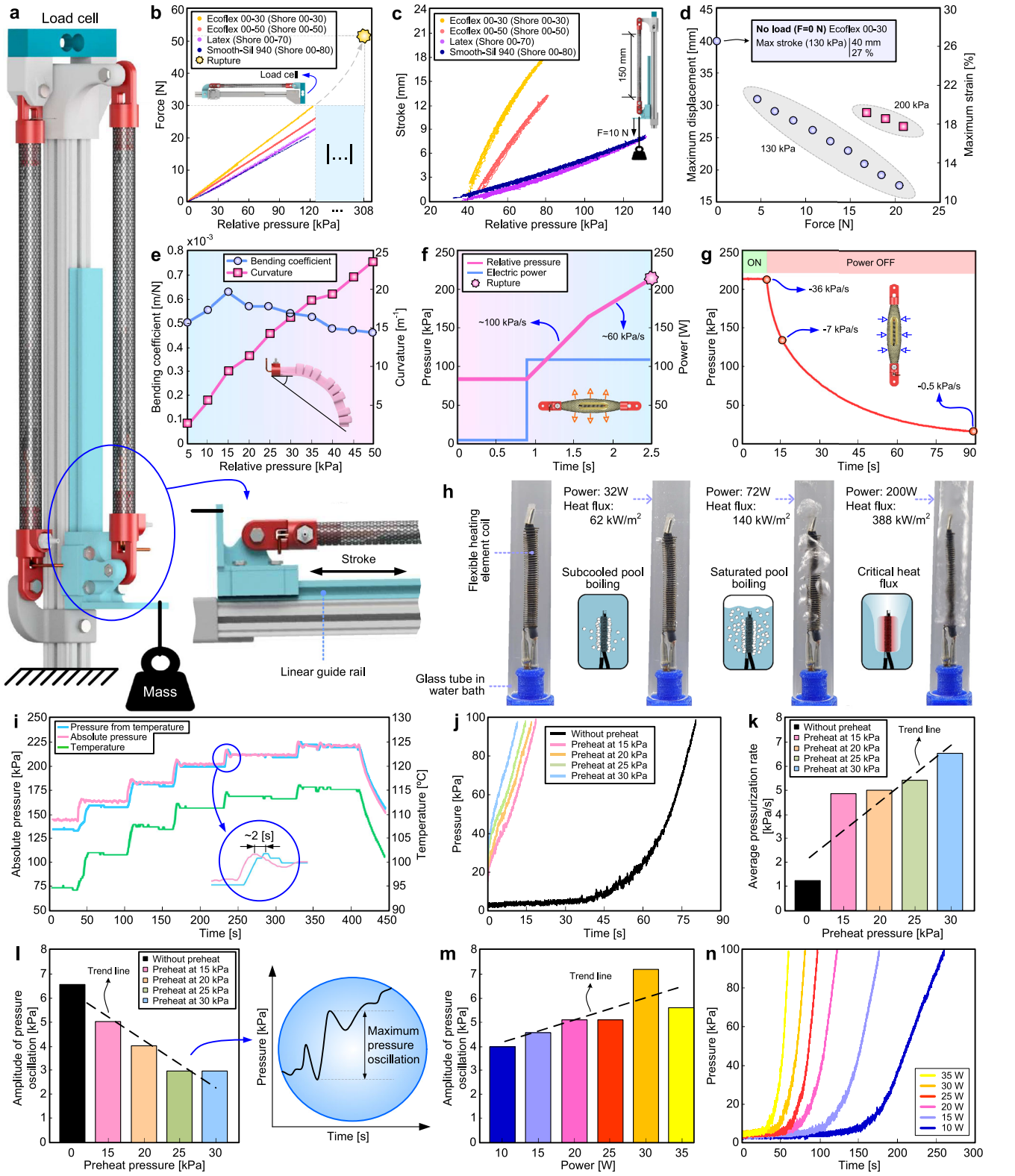

pressure[71], remained relatively stable with an average value of 0.5×10^{-3} m/N at pressures up to 50 kPa (Fig. 3e). At 50 kPa the actuator reaches its maximum design bending angle of 90 degrees.

Performance limits

We proceeded to evaluate the limits of the proposed design by subjecting a linear soft actuator to an isometric shock test. Starting from a preheated state, the actuator was supplied with a short-term electric impulse corresponding to 110 W of electric power. During this test, a pressurization rate of 100 kPa/s was achieved, (Fig. 3f). The actuator experienced an overpressure failure at 210 kPa without any signs of burned elements, suggesting that CHF conditions may not have been achieved even at these power settings. At 110 W, the heat flux on the heating element's surface is ~213 kW/m². We then tested the same heating element inside a transparent glass tube, under conditions similar to those expected inside the actuator, to visually confirm the

Fig. 3 | Experimental tests and actuator characterization. a Setup used for isometric and isotonic tests. **b** Blocked force of linear actuators made using different elastomers, tested under isometric conditions without prestrain. **c** Strain of linear actuators under a constant load of 10 N. **d** Maximum strain of a linear actuator made from Ecoflex 00–30 under multiple loads while operating at two different pressures. **e** Curvature and bending coefficient of a bending actuator. The bending coefficient was calculated in accordance with the method originally proposed by Gorissen et al.[71]. **f** Electric power, internal pressure and internal pressure rate of a linear actuator during an impulse shock, tested under isometric conditions without prestrain. **g** Internal pressure during the cooling down of a linear actuator, tested under isometric conditions without prestrain. **h** Demonstration of boiling regimes occurring at different heat fluxes. Tested using an actuator heating element and a water-filled transparent glass tube made to be geometrically identical to an actuator's silicone soft structure. **i** Saturation pressure calculated from internal temperature measurements compared against actual internal pressure. **j** Pressure evolution at a 25 W constant power setting, with and without preheating. Test under isometric conditions without prestrain. **k** Average pressurization rate at 25 W, with and without preheating. Test under isometric conditions without prestrain. **l** Amplitude of pressure oscillations at 25 W, with and without preheating, and tested under isometric conditions without prestrain. The inset shows the definition of pressure oscillation. **m** The amplitude of a linear actuator's pressure oscillations at different power settings under isometric conditions without prestrain. **n** Internal pressure of a linear actuator, at different power settings, under isometric conditions without prestrain. Unless otherwise stated, all tests were conducted with linear actuators made from Ecoflex 00–30.

onset of CHF conditions. In this case, CHF was achieved only at ~388 kW/m² (Fig. 3h). Knowing the maximum pressurization rate to be at least 100 kPa/s, we then pressurized an identical prototype to the same pressure of 210 kPa and recorded its internal pressure during the cooling down phase (Fig. 3g). The highest magnitude of depressurization rate, 35.8 kPa/s, was measured at 210 kPa, reducing to 7.1 kPa/s at 130 kPa and 0.5 kPa/s at 20 kPa. The results demonstrate the achievable pressurization performance and highlight a limiting factor, the rate of heat dissipation.

Control strategy

Previous liquid-gas phase transition actuators have been controlled using PI and ON-OFF controllers, with feedback based on pressure, strain, force or temperature[51,53–55,72]. Determining an appropriate feedback signal for a class of high-power actuators is a key factor. In a McKibben actuator, force is a function of both strain and pressure. Therefore, a single feedback signal of force or strain would not allow for the effective detection of overpressure events.

Temperature and pressure are both thermodynamic state variables, so one can be derived from the other assuming steady state and saturated fluid conditions. We evaluated the feasibility of temperature-based control by powering up a linear actuator under isometric conditions while capturing internal temperatures and pressures using the actuator's built-in sensors. We then calculated the fluid saturation pressure from the temperature measurements. An offset of 13 °C was used during this calculation to account for internal temperature gradients. This offset adjustment allows for reasonable pressure tracking using temperature measurements, but temperature signals lagged behind pressure feedback by ~2 s due to the thermal masses present (Fig. 3i). Having demonstrated the potential for pressurization rates of 100 kPa/s, we consider feedback signal lags over 100 ms to be incompatible with high power operation. The conclusion is that pressure feedback is, in fact, the preferred option.

We also evaluated whether the onset of CHF could be detected by monitoring the electrical resistance of the actuator. Our hypothesis was that a significant temperature increase in the coil's surface would result in an abrupt variation in the coil's electrical resistance value, which would be detected by the controller and used to limit electrical supply during high-power short-term impulses. We achieved mixed results. Data recovered during the CHF experiment in Fig. 3h, where the coil was statically assembled inside a rigid test chamber, does show an abrupt change in electrical resistance occurring at the precise instant when we can visually confirm the onset of CHF. However, when analysing similar data obtained from real actuators, we could not reliably observe this phenomenon due to an excess of noise in the data. Although we could not determine the origin of this noise, it may be related to thermal strain of the crimp connections used to connect the coil to the internal electrical connections (Supplementary Note 2).

An effective control strategy must also ensure that the actuators are kept in thermodynamically saturated conditions. We achieved this by setting a minimum standby pressure that is higher than the atmospheric pressure. Four different standby pressure values were tested, ranging from 0 kPa to 30 kPa, by pressurizing a linear actuator under a constant power of 25 W for 60 s. The results showed that preheating effectively reduces control lag (Fig. 3j), increases pressurization rates (Fig. 3k), while simultaneously reducing the amplitude of pressure oscillations (Fig. 3l). The reduction in pressure oscillations due to preheating supports the hypothesis that unsaturated thermodynamic conditions are the underlying cause of actuator vibrations. However, since higher standby pressures reduce the operating range, we settled on a standby pressure of 20 kPa as a compromise solution.

Additionally, we verified that operating under lower power settings also reduces pressure oscillations (Fig. 3m). Although a reduction of power would inevitably limit the actuator's pressurization and strain rate performance (Fig. 3n), this effect can be exploited to further reduce boiling instabilities during the initial preheating stage, without compromising performance under normal operating conditions.

The hardware implementation of the non-linear control strategy (Fig. 4a) is detailed in "Methods" section. The control strategy applies an ON-OFF controller to preheat actuators with a low constant heat flux of ~16 kW/m², until their standby pressure is reached. At this point, a PI controller takes over and is used to track pressure values within the actuator's operating range (Fig. 4b). The PI controller can impose higher heat fluxes of up to 64 kW/m² under normal operating conditions, a value that was empirically defined according to conservative safety requirements and the results of material testing available in the Supplementary Note 4. Results show the controller's ability to converge to either target pressures or displacements (Fig. 4c, d, and Supplementary Movie 2).

Robot prototypes

The performance of our soft actuators combined with their compact form factor motivated us to explore how this technology can be integrated into different soft robots. We started by developing a biomimetic hand powered by three linear soft actuators (Fig. 5a), demonstrating how compliant soft actuators can be integrated into an otherwise non-compliant mechanical system. The actuators are linked to the finger joints using tendons made of nylon wire. A compact pulley system provides a 1:2 transmission ratio, duplicating the linear displacement provided by the actuators. A set of springs provides the tension required to return the actuators back to their extended position. Two actuators control the thumb and index fingers independently, while a third actuator controls the middle, ring and little fingers simultaneously. The fingers can close approximately five times faster than they can open (Fig. 5b), highlighting once again the limitation imposed by the rate of heat dissipation. The hand is capable of grasping objects of various shapes and sizes while benefiting from the compliance inherent to soft actuators (Fig. 5c and Supplementary Movie 3).

We then proceeded to demonstrate a soft gripping task by building an electric soft gripper powered by three bending actuators (Fig. 5d). Not accounting for the actuators themselves, the design and

https://doi.org/10.1038/s41467-025-59023-7

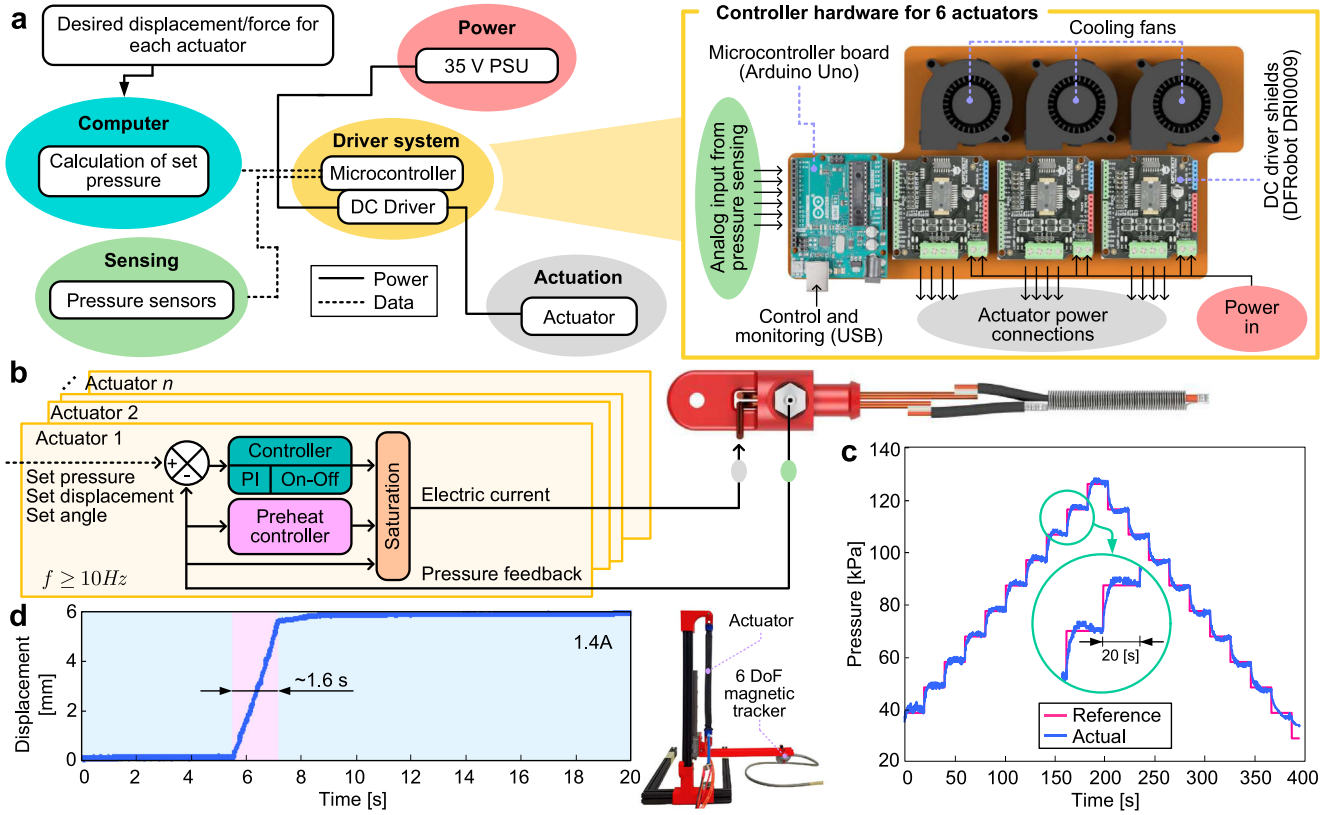

Fig. 4 | Actuator control architecture and main elements. a Controller hardware, system architecture and connection diagram. **b** Actuator controller based on PI or the On-Off method. **c** Control results for step target pressure (incremental steps of 10 kPa each lasting 20 s). The reduction in depressurization rates becomes apparent at pressures below 40 kPa. **d** The optimized PI-based actuator displacement controller takes ~1.6 s to reach a set displacement of 6 mm. Displacement values were obtained using a 6 Degrees of Freedom (DoF) magnetic tracker.

assembly of this gripper was completed in <1 h, demonstrating the development efficiency enabled by general-use soft actuators. The gripper, attached to a robot, successfully performed pick-and-place tasks using fruit models of varying weights, sizes and geometries from the Yale-CMU-Berkeley (YCB) Object and Model Set (Fig. 5e, f, and Supplementary Video 4). Successful grasping of all models was achieved at pressures >60 kPa (Fig. 5g).

Finally, to demonstrate the potential of these actuators in a complex locomotion task, we designed and implemented Bixo, an electric soft quadruped robot powered by liquid-gas phase transition. Bixo is a development platform that can perform complex locomotion tasks such as climbing tubes and crawling along trees. We designed Bixo to enable rapid replacement of the mechatronic components, specifically the sliding structure and the five actuators. Four of these actuators are bending-type soft actuators, and the fifth is a DC motor with a reduction gear drive to actuate the sliding structure (SS) through a lead screw (Fig. 6a and Supplementary Note 8). Bixo's legs adjust to circular profiles, functioning as grippers, one for the back legs (BL) and another for the front legs (FL) (Fig. 6b). Locomotion on an inclined tube is achieved through a cyclic process in which (i) the robot's FL close to grasp the circular profile and fix the robot in place, (ii) the DC motor actuates the lead screw to position the open BL, (iii) the BL close to grasp the circular profile and fix the robot in place, (iv) the FL open to release the circular profile, and (v) the DC motor actuates the lead screw again to reposition the FL (Fig. 6c and Supplementary Movie 5). The first complete cycle of the actuation pattern was completed in ~80 s and after stabilization a faster cycle of ~25 s is achieved, considering a set pressure of ~60 kPa for both the BL and FL (Fig. 6d). This decrease in cycle rate is caused by the asymmetry between the pressurization and depressurization rates of the actuators, resulting in each subsequent cycle to begin at a higher pressure than the previous one, thereby requiring less time to reach the pressure needed for grasping the tube. This effect persists until the starting pressure of each cycle matches the maximum pressure at which the robot can release its grasp on the tube. At this point, the cycle rate stabilizes and ceases to decrease (Fig. 6d). Bixo demonstrated the capability to crawl on a horizontal tree trunk, showing compliance with the uncertainty of the rough surface of the trunk (Fig. 6e, f, and Supplementary Movie 5). This robotic platform can be equipped with multiple sensors and sets a solid foundation for the continuous development of untethered robots powered by liquid-gas phase transition actuators.

Discussion

This work brings to light the hidden capabilities of high-power electric liquid-gas phase transition actuators. We introduce a soft actuator design capable of pressurization rates of over 100 kPa/s, and contractile strain rates of over 16%/s. We propose a comprehensive selection method for working fluids that allows actuators to meet specific application requirements. The instability responsible for actuator vibration at high power settings was also identified and addressed using a non-linear control approach.

The standardization of soft robotic technologies, including soft actuators, is a challenge that should be addressed in the coming years as an enabling strategy to increase the availability, functionality, and flexibility of increasingly complex robots. Standardizing electric soft actuators will be particularly challenging due to the difficulties of transmitting mechanical energy through soft materials. Actuators will need to be adaptable and capable of delivering mechanical energy in its final form without depending on the stiffness of traditional

https://doi.org/10.1038/s41467-025-59023-7

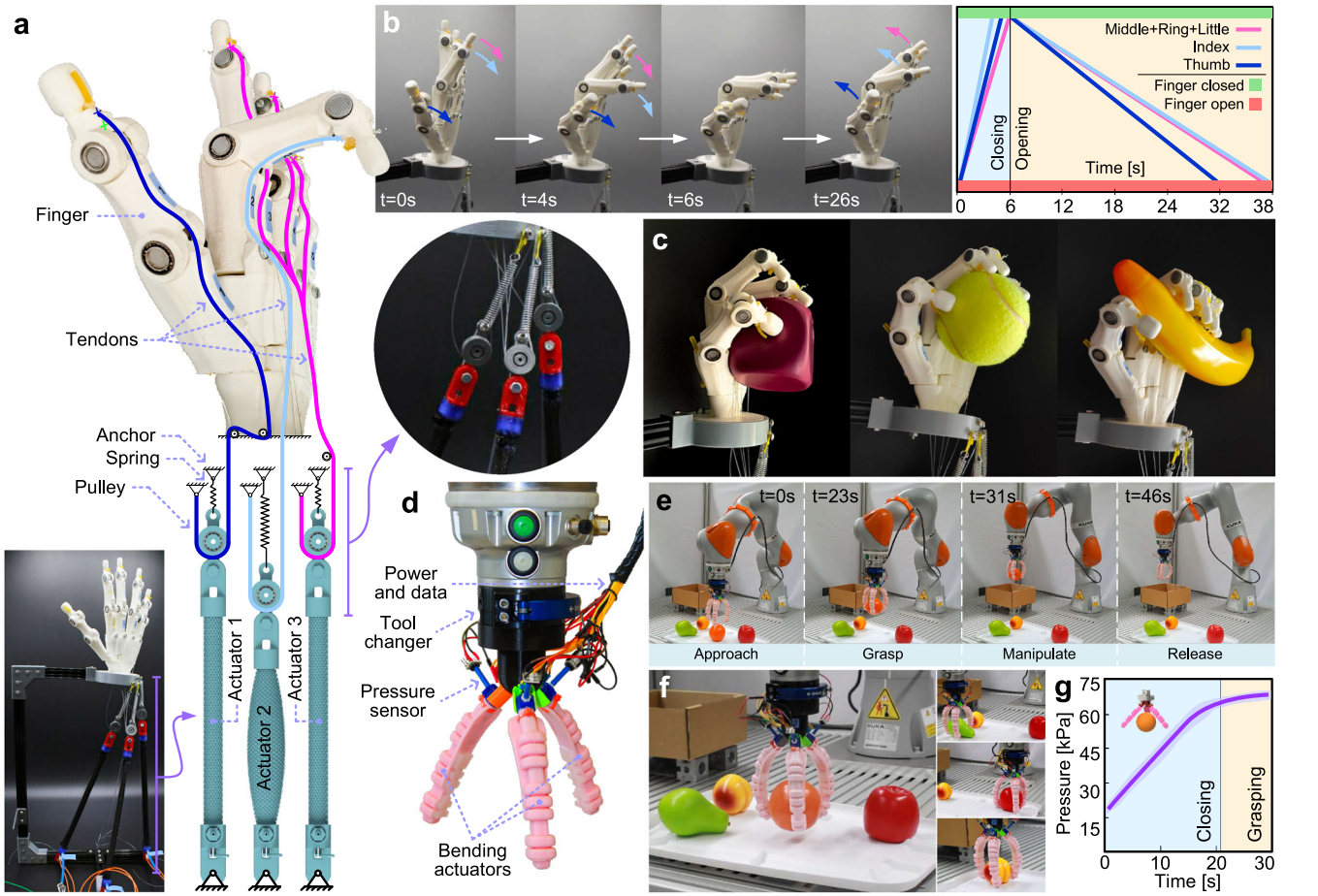

Fig. 5 | Biomimetic hand and electric soft gripper. a Tendon-driven biomimetic hand powered by three linear actuators using a spring pulley mechanism. The soft actuators provide compliant yet precise actuation. **b** The fingers' motion and the hand's opening/closing time individualized for each finger. **c** Biomimetic hand grasping various objects. **d** Soft gripper composed of three bending-type actuators attached to a collaborative robot flange. **e** Together, the robot and the gripper can perform pick-and-place operations. **f** The gripper can grasp and manipulate fruit models of varying weight and geometry. **g** Grasping an orange is achieved at pressures > 60 kPa and takes ~20 s with the actuators operating at 20 W.

mechanical transmission mechanisms. Our actuator's modular design and physical adaptability facilitate their integration into innovative untethered robotic systems. Moreover, they are fabricated using off-the-shelf materials, electronics, and manufacturing equipment.

Regarding the limited depressurization rates observed throughout this work, our results suggest two possible strategies for future improvement. The first strategy is to increase the area to volume ratio of the actuators, through miniaturization. Heat energy stored in an actuator at a given temperature is proportional to its volume, while the rate of convective heat dissipation is proportional to its surface area. Accordingly, by increasing the area-to-volume ratio, a greater proportion of the total stored latent heat energy could be dissipated during the same time period. A second strategy for improving depressurization rates would be to shift the entire operating pressure range towards higher values, simultaneously increasing both the preheated standby and maximum operating pressures, at the cost of a reduced factor of safety. This strategy is based on our observation that higher pressures lead to higher depressurization rates. However, operating at higher pressures without reducing the actuator's displacement range would require the use of preloading mechanisms, adding complexity to the design. Additionally, little is known about the life expectancy of liquid-gas phase transition actuators. During this work, the actuators endured over a 10^3 actuation cycles over 10 months of testing, but their actual life expectancy and modes of failure remain to be studied.

Without overlooking the limitations in efficiency imposed by electrothermal soft actuation, we argue that liquid-gas soft actuators offer a combination of performance and adaptability that should not be ignored and could potentially result in significant gains in system-wide efficiency. An example of this can be seen in Bixo, which required an average of 50 W of power across all actuators during its tube-climbing task. Although this value is difficult to benchmark due to the unique nature of the robot, it is plausible to argue that it is within the same order of magnitude as what would be expected of a similarly sized non-soft robot, performing a similar task. This is a key contribution towards reaching the inflection point where soft robots become an enticing alternative to rigid robotic systems, moving them from the laboratory into our daily lives.

Methods

Materials

The actuator end terminals were 3D printed in thermoplastic polyurethane (TPU 98 A, RS PRO, United Kingdom) due to its high softening point of 138 °C. The heating element coil is made of FeCrAl wire (Kanthal A, Kanthal, Sweden) due to its higher electrical resistivity when compared to other common alloys such as NiCr, NiFe or CuNi. This enables the actuators to operate with lower currents, thereby reducing electrical losses. While NiCr alloys present better wet corrosion resistance, the aluminum oxide (Al_2O_3) formed on FeCrAl has better adhesion to the alloy's surface and it is a better electrical

https://doi.org/10.1038/s41467-025-59023-7

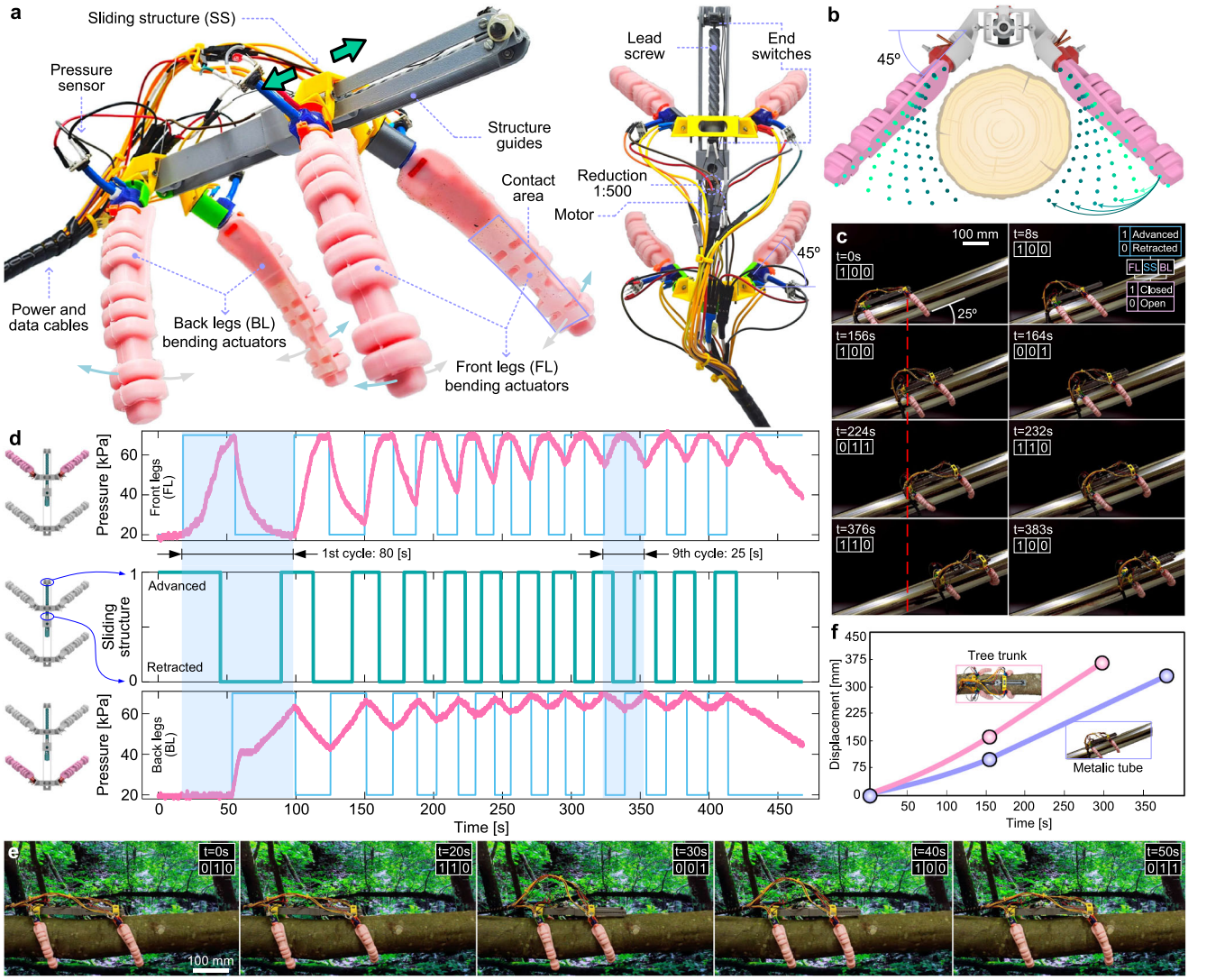

Fig. 6 | Electric-driven soft quadruped robot Bixo. a The Bixo design includes two bending-type actuators for each of the back and front legs, and a DC motor to actuate the lead screw that operates the sliding structure. **b** Robot legs assembled to grasp circular profiles. **c** Locomotion on an inclined tube. **d** Locomotion cyclic pattern considering a set pressure of ~60 kPa for both BL and FL. **e** Locomotion on an unstructured tree trunk. **f** Robot displacement in both environments.

insulator when compared to chromium oxide (Cr_2O_3) formed on NiCr. The actuator's soft structures were fabricated using platinum-cured silicones. Unless specified otherwise, linear actuators were made with Ecoflex 00–30 (Smooth-On, USA). Bending actuators were fabricated using Smooth-Sil 940 (Smooth-On, USA), with an additional layer of Ecoflex 00–30 to increase friction, which is required for grasping applications. The linear actuator's braided sleeve is made of Polyethylene Terephthalate (PET) (article. no. 06240405010, SES Sterling, France). The rigid structural elements of the robot prototypes were 3D printed using acrylonitrile butadiene styrene (ABS, RS PRO, United Kingdom).

Fabrication of actuator's heating element

The heating element coil is wound around a high-temperature silicone-insulated electric wire and connected to copper terminals on one side using an electrical wire ferrule. The high temperature wire is used to connect the opposite end of the coil. Copper terminals are passed through the TPU structural terminals and sealed using cyanoacrylate adhesive (401, Loctite, Germany). Details of the fabrication process are available in the Supplementary Note 2.

Fabrication of the actuator's soft structures

The linear actuator's soft structure is a cylindrical tube, 170 mm long, with an internal diameter of 6 mm and an external diameter of 9 mm. It was cast using 3D printed molds and aluminum cores. The tube is then sheathed with the braided sleeve. The geometric parameters of the braid, which influence the theoretical maximum actuator displacement, are as detailed in Supplementary Note 5. The bending actuator variant features a complex-shaped hollow soft structure, which is cast using 3D printed molds and a water-soluble hollow core. The core is 3D printed in polyvinyl alcohol (Smartfil PVA, Smart Materials 3D, Spain) and later dissolved in a water bath at 60 °C. To expedite the dissolution process, heated water is circulated under pressure through the hollow core using water pumps[10]. The molds, water-soluble cores, and robot components were 3D printed on a commercially available FFF 3-axis single-nozzle machine (Prusa i3 MK3S + , Prusa, Czechia). The detailed fabrication process of both the linear and bending actuator variants is detailed in Supplementary Note 3.

Control and monitoring elements

An actuator control unit is composed of an off-the-shelf micro-controller (Arduino Uno, Arduino, Italy) and DC motor driver shields

based on the L298n full-bridge driver (DRI0009, DFRobot, China) (Fig. 4a). The controller can drive up to 6 actuators simultaneously, at currents of up to 2 A each. A high-power version of the controller, used for the isometric shock test, was also assembled by replacing the DC motor shields with 40 A DC solid-state relays. A pressure sensor is installed in each actuator to provide pressure feedback (ABP-DANV060PGAA5, Honeywell, USA). The microcontroller receives feedback from the sensors and sends commands to the actuator while running the proposed controllers. The graphical user interface (GUI) and wiring diagram are detailed in Supplementary Figs. 14 and 15.

Characterization experiments

Isometric and isotonic experimental tests were conducted at room temperature (20 to 25 °C, 1 atm). Force values were acquired using a 5 kg capacity load cell (TAL220B, HT Sensor Technology Co, China). Internal actuator temperature was monitored using a digital temperature sensor (DS18B20, Maxim Integrated, USA) installed in the actuators solely for characterization purposes. This sensor is not required during normal operation of the actuators. Displacement feedback was captured using a 6 DoF magnetic tracker (Liberty, Polhemus, USA) and bending angles were measured using a custom MATLAB video processing program. Data analysis was conducted using a custom python interface that reads data from the microcontroller. A validated static model, which associates pressures, displacements, and static forces, was developed using data from isotonic tests, detailed in Supplementary Note 6.

Data availability

All data supporting the findings and conclusions of this study are provided in the main text and supplementary materials[73–77]. Data necessary for replicating the actuators and robot prototypes are also included. For additional information, please contact the corresponding author. Updated drawings and computer code are available in the GitHub repository https://github.com/softrobotic/bixo, and the Zenodo repository https://doi.org/10.5281/zenodo.15013682.

References

1. Li, M., Pal, A., Aghakhani, A., Pena-Francesch, A. & Sitti, M. Soft actuators for real-world applications. *Nat. Rev. Mater.* **7**, 235–249 (2022).
2. Laschi, C. & Mazzolai, B. Lessons from animals and plants: the symbiosis of morphological computation and soft robotics. *IEEE Robot. Autom. Mag.* **23**, 107–114 (2016).
3. Katzschmann, R. K., DelPreto, J., MacCurdy, R. & Rus, D. Exploration of underwater life with an acoustically controlled soft robotic fish. *Sci. Robot.* **3**, 3449 (2018).
4. Chen, Y. et al. Controlled flight of a microrobot powered by soft artificial muscles. *Nature* **575**, 324–329 (2019).
5. Ren, Z., Hu, W., Dong, X. & Sitti, M. Multi-functional soft-bodied jellyfish-like swimming. *Nat. Commun.* **10**, 2703 (2019).
6. Wehner, M. et al. An integrated design and fabrication strategy for entirely soft, autonomous robots. *Nature* **536**, 451–455 (2016).
7. Han, J. et al. Untethered soft actuators by liquid–vapor phase transition: remote and programmable actuation. *Adv. Intell. Syst.* **1**, 1900109 (2019).
8. Jones, T. J., Jambon-Puillet, E., Marthelot, J. & Brun, P.-T. Bubble casting soft robotics. *Nature* **599**, 229–233 (2021).
9. Rus, D. & Tolley, M. T. Design, fabrication and control of soft robots. *Nature* **521**, 467–475 (2015).
10. Silva, A., Fonseca, D., Neto, D. M., Babcinschi, M. & Neto, P. Integrated design and fabrication of pneumatic soft robot actuators in a single casting step. *Cyborg Bionic Syst.* **5**, 0137 (2024).
11. Lee, S. et al. A transparent bending-insensitive pressure sensor. *Nat. Nanotechnol.* **11**, 472–478 (2016).
12. Truby, R. L., Chin, L., Zhang, A. & Rus, D. Fluidic innervation sensorizes structures from a single build material. *Sci. Adv.* **8**, 32 (2022).
13. Tan, P. et al. Solution-processable, soft, self-adhesive, and conductive polymer composites for soft electronics. *Nat. Commun.* **13**, 1–12 (2022).
14. Tavakoli, M. et al. 3R electronics: scalable fabrication of resilient, repairable, and recyclable soft-matter electronics. *Adv. Mater.* **34**, e2203266 (2022).
15. Hawkes, E. W., Majidi, C. & Tolley, M. T. Hard questions for soft robotics. *Sci. Robot.* **6**, 1–6 (2021).
16. Rich, S. I., Wood, R. J. & Majidi, C. Untethered soft robotics. *Nat. Electron.* **1**, 102–112 (2018).
17. Li, S., Vogt, D. M., Rus, D. & Wood, R. J. Fluid-driven origami-inspired artificial muscles. *Proc. Natl Acad. Sci.* **114**, 13132–13137 (2017).
18. Zhai, Y. et al. Desktop fabrication of monolithic soft robotic devices with embedded fluidic control circuits. *Sci. Robot.* **8**, 1–14 (2023).
19. Higueras-Ruiz, D. R., Shafer, M. W. & Feigenbaum, H. P. Cavatappi artificial muscles from drawing, twisting, and coiling polymer tubes. *Sci. Robot.* **6**, eabd5383 (2021).
20. Onal, C. D., Chen, X., Whitesides, G. M. & Rus, D. Soft mobile robots with on-board chemical pressure generation. *Springe. Tracts Adv. Robot.* **100**, 525–540 (2017).
21. Bartlett, N. W. et al. A 3D-printed, functionally graded soft robot powered by combustion. *Science* **349**, 161–165 (2015).
22. Yang, X., Chang, L. & Pérez-Arancibia, N. O. An 88 milligram insect-scale autonomous crawling robot driven by a catalytic artificial muscle. *Sci. Robot.* **5**, 1–14 (2020).
23. He, Q. et al. Electrospun liquid crystal elastomer microfiber actuator. *Sci. Robot.* **6**, 887–890 (2021).
24. Pantula, A. et al. Untethered unidirectionally crawling gels driven by asymmetry in contact forces. *Sci. Robot.* **7**, 22–29 (2022).
25. Hu, Z., Zhang, Y., Jiang, H. & Lv, J. Bioinspired helical-artificial fibrous muscle structured tubular soft actuators. *Sci. Adv.* **9**, eadh3350 (2023).
26. Kim, Y., Yuk, H., Zhao, R., Chester, S. A. & Zhao, X. Printing ferromagnetic domains for untethered fast-transforming soft materials. *Nature* **558**, 274–279 (2018).
27. Boyvat, M., Vogt, D. M. & Wood, R. J. Ultrastrong and high-stroke wireless soft actuators through liquid–gas phase change. *Adv. Mater. Technol.* **4**, 1–6 (2019).
28. Li, C. et al. Fast and programmable locomotion of hydrogel-metal hybrids under light and magnetic fields. *Sci. Robot.* **5**, eabb9822 (2020).
29. Meder, F., Naselli, G. A., Sadeghi, A. & Mazzolai, B. Remotely light-powered soft fluidic actuators based on plasmonic-driven phase transitions in elastic constraint. *Adv. Mater.* **31**, e1905671 (2019).
30. Zadan, M. et al. Liquid crystal elastomer with integrated soft thermoelectrics for shape memory actuation and energy harvesting. *Adv. Mater.* **34**, 2200857 (2022).
31. Fowler, H. E., Rothemund, P., Keplinger, C. & White, T. J. Liquid crystal elastomers with enhanced directional actuation to electric fields. *Adv. Mater.* **33**, 1–8 (2021).
32. Rajappan, A., Jumet, B. & Preston, D. J. Pneumatic soft robots take a step toward autonomy. *Sci. Robot.* **6**, 1–3 (2021).
33. Conrad, S. et al. 3D-printed digital pneumatic logic for the control of soft robotic actuators. *Sci. Robot.* **9**, eadh4060 (2024).
34. Hubbard, J. D. et al. Fully 3D-printed soft robots with integrated fluidic circuitry. *Sci. Adv.* **7**, eabe5257 (2021).
35. Drotman, D., Jadhav, S., Sharp, D., Chan, C. & Tolley, M. T. Electronics-free pneumatic circuits for controlling soft-legged robots. *Sci. Robot.* **6**, eaay2627 (2021).
36. Kovacs, G., Düring, L., Michel, S. & Terrasi, G. Stacked dielectric elastomer actuator for tensile force transmission. *Sensors Actuators. A Phys.* **155**, 299–307 (2009).

37. Acome, E. et al. Hydraulically amplified self-healing electrostatic actuators with muscle-like performance. *Science* **359**, 61–65 (2018).
38. Sîrbu, I. D. et al. Electrostatic bellow muscle actuators and energy harvesters that stack up. *Sci. Robot.* **6**, 1–12 (2021).
39. Wu, Y. et al. Insect-scale fast moving and ultrarobust soft robot. *Sci. Robot.* **4**, 32 (2019).
40. Gao, X. et al. Piezoelectric actuators and motors: materials, designs, and applications. *Adv. Mater. Technol.* **5**, 1–26 (2020).
41. Xu, Y., Wang, T. & Wang, Z. Electrically actuated soft actuator integrated with an electrochemical reactor. *Extrem. Mech. Lett.* **56**, 101891 (2022).
42. Johannisson, W., Harnden, R., Zenkert, D. & Lindbergh, G. Shape-morphing carbon fiber composite using electrochemical actuation. *Proc. Natl Acad. Sci. USA* **117**, 7658–7664 (2020).
43. Xia, X. et al. Electrochemically reconfigurable architected materials. *Nature* **573**, 205–213 (2019).
44. Chen, S. et al. Molecular-level methylcellulose/MXene hybrids with greatly enhanced electrochemical actuation. *Adv. Mater.* **34**, 1–13 (2022).
45. Liu, Q. et al. Micrometer-sized electrically programmable shape-memory actuators for low-power microrobotics. *Sci. Robot.* **6**, 1–9 (2021).
46. Shu, J. et al. A Liquid Metal Artificial Muscle. *Adv. Mater.* **33**, 1–10 (2021).
47. Liao, J. & Majidi, C. Soft actuators by electrochemical oxidation of liquid metal surfaces. *Soft Matter* **17**, 1921–1928 (2021).
48. Chen, S., Tan, M. W. M., Gong, X. & Lee, P. S. Low-voltage soft actuators for interactive human–machine interfaces. *Adv. Intell. Syst.* **4**, 2100075 (2022).
49. Sun, J., Tighe, B., Liu, Y. & Zhao, J. Twisted-and-coiled actuators with free strokes enable soft robots with programmable motions. *Soft Robot.* **8**, 213–225 (2021).
50. He, Q. et al. Electrically controlled liquid crystal elastomer–based soft tubular actuator with multimodal actuation. *Sci. Adv.* **5**, 1–8 (2019).
51. Kang, B., Lim, S., Kim, H. & Wang, W. D. Electrically driven robotic pistons exploiting liquid-vapor phase transition for underwater applications. *IEEE Robot. Autom. Lett.* **8**, 2118–2125 (2023).
52. Evenchik, A. L., Kane, A. Q., Oh, E. B. & Truby, R. L. Electrically controllable materials for soft, bioinspired machines. *Annu. Rev. Mater. Res.* **53**, 225–251 (2023).
53. Mirvakili, S. M., Sim, D., Hunter, I. W. & Langer, R. Actuation of untethered pneumatic artificial muscles and soft robots using magnetically induced liquid-to-gas phase transitions. *Sci. Robot.* **5**, 1–10 (2020).
54. Bilodeau, R. A., Miriyev, A., Lipson, H. & Kramer-Bottiglio, R. All-soft material system for strong soft actuators. In *2018 IEEE International Conference on Soft Robotics (RoboSoft)* 288–294 (IEEE, 2018).
55. Narumi, K. et al. Liquid pouch motors: printable planar actuators driven by liquid-to-gas phase change for shape-changing interfaces. *IEEE Robot. Autom. Lett.* **5**, 3915–3922 (2020).
56. Miriyev, A., Stack, K. & Lipson, H. Soft material for soft actuators. *Nat. Commun.* **8**, 596 (2017).
57. Miriyev, A., Caires, G. & Lipson, H. Functional properties of silicone/ethanol soft-actuator composites. *Mater. Des.* **145**, 232–242 (2018).
58. Zhang, B., Gong, S., Dong, S., Xiong, Z. & Guo, Q. Experimental investigation on vibration characteristics of subcooled and saturated pool boiling. *Appl. Therm. Eng.* **218**, 119297 (2023).
59. Pattanayak, B. & Kothadia, H. Experimental study of critical heat flux during pool boiling on mini tubes: effect of subcooling, orientation, and dimensions. *Heat. Transf. Eng.* **43**, 896–921 (2022).
60. Decroly, G. et al. Optimization of phase-change material–elastomer composite and integration in kirigami-inspired voxel-based actuators. *Front. Robot. AI* **8**, 1–12 (2021).
61. Mosadegh, B. et al. Pneumatic networks for soft robotics that actuate rapidly. *Adv. Funct. Mater.* **24**, 2163–2170 (2014).
62. Cho, H. J., Preston, D. J., Zhu, Y. & Wang, E. N. Nanoengineered materials for liquid–vapour phase-change heat transfer. *Nat. Rev. Mater.* **2**, 16092 (2016).
63. Garrad, M., Soter, G., Conn, A. T., Hauser, H. & Rossiter, J. Driving soft robots with low-boiling point fluids. in *2019 2nd IEEE International Conference on Soft Robotics (RoboSoft)* 74–79 (IEEE, 2019).
64. Noguchi, T. & Tsumori, F. Soft actuator with large volumetric change using vapor–liquid phase transition. *Jpn. J. Appl. Phys.* **59**, SIIL08 (2020).
65. Xia, B. et al. Improving the actuation speed and multi-cyclic actuation characteristics of silicone/ethanol soft actuators. *Actuators* **9**, 62 (2020).
66. Miriyev, A., Trujillo, C., Caires, G. & Lipson, H. Rejuvenation of soft material-actuator. *MRS Commun.* **8**, 556–561 (2018).
67. Liang, G. & Mudawar, I. Pool boiling critical heat flux (CHF)—part 1: review of mechanisms, models, and correlations. *Int. J. Heat. Mass Transf.* **117**, 1352–1367 (2018).
68. Chou, C. P., Hannaford, B., Ching-Ping, C. & Hannaford, B. Measurement and modeling of McKibben pneumatic artificial muscles. *IEEE Trans. Robot. Autom.* **12**, 90–102 (1996).
69. Tondu, B. & Lopez, P. Modeling and control of McKibben artificial muscle robot actuators. *IEEE Control Syst.* **20**, 15–38 (2000).
70. Bruder, D. & Wood, R. J. The chain-link actuator: exploiting the bending stiffness of mckibben artificial muscles to achieve larger contraction ratios. *IEEE Robot. Autom. Lett.* **7**, 542–548 (2022).
71. Gorissen, B. et al. Elastic inflatable actuators for soft robotic applications. *Adv. Mater.* **29**, 1604977 (2017).
72. Higashijima, K., Kato, T., Sakuragi, K., Sato, T. & Ono, M. Development of manipulator using a gas–liquid phase-change actuator. *JFPS Int. J. Fluid Power Syst.* **11**, 70–74 (2019).
73. Watson, K. M. Thermodynamics of the liquid state: generalized prediction of properties. *Ind. Eng. Chem.* **35**, 398–406 (1943).
74. Buck, A. L. New equations for computing vapor pressure and enhancement factor. *J. Appl. Meteorol. Climatol.* **20**, 1527–1532 (1981).
75. Coker, A. K. Ludwig's *Applied Process Design for Chemical and Petrochemical Plants* 4th edn, Vol. 1257 (Gulf Professional Publishing, 2010).
76. Haines, C. S. et al. Artificial muscles from fishing line and sewing thread. *Sci* **343**, 868–872 (2014).
77. Duduta, M., Hajiesmaili, E., Zhao, H., Wood, R. J. & Clarke, D. R. Realizing the potential of dielectric elastomer artificial muscles. *Proc. Natl Acad. Sci. USA* **116**, 2476–2481 (2019).

Acknowledgements

We thank A. Silva and P. Matos for the valuable discussions and suggestions on the fabrication of soft actuators. We also thank P. Costa for the technical support in the realization of the robot's experimental tests. This work was supported by the Portuguese Foundation for Science and Technology grant UIDB/00285/2020 (P.N.), LA/P/0112/2020 (P.N.), and 2022.13512.BD (D.F.).

Author contributions

Conceptualization: D.F., P.N. Methodology: D.F., P.N. Investigation: D.F. Visualization: D.F., P.N. Funding acquisition, project administration and supervision: P.N. Writing—original draft: D.F. Writing—review and editing: P.N.

Competing interests

The authors declare no competing interests.

Additional information

Supplementary information The online version contains supplementary material available at https://doi.org/10.1038/s41467-025-59023-7.

Correspondence and requests for materials should be addressed to P. Neto.

Peer review information *Nature Communications* thanks Richard Suphapol Diteesawat and Martin Garrad for their contribution to the peer review of this work. A peer review file is available.